Design and Analysis of Piezoelectric Metamaterial Beams With Synthetic Impedance Shunt Circuits

Christopher Sugino, Massimo Ruzzene, and Alper Erturk

***Abstract*—We present an electromechanical modeling framework and a detailed numerical investigation for the design and analysis of piezoelectric metamaterial beams whose unit cells with segmented electrode pairs are shunted to synthetic impedance circuits. This framework aims to extend the well-studied locally resonant piezoelectric metamaterials and resulting finite metastructures with specified boundary conditions to novel concepts beyond bandgaps associated with simple inductive shunts. Overcoming the bandgap limitations of the locally resonant design requires more advanced considerations in the electrical domain. To this end, we bridge piezoelectric metamaterials and synthetic impedance shunts, and present a general design and analysis framework along with numerical case studies. A general procedure is implemented based on the root locus method for choosing the shunt circuit impedance, with an emphasis on vibration attenuation and practical design considerations. Case studies are presented for systems with locally resonant bandgaps with or without negative capacitance, as well as systems with multiple distinct bandgaps, and the necessary shunt admittance is derived for each case. Simulations are performed for a typical finite meta material beam with synthetic impedance shunts, accounting for the finite sampling rate and circuit dynamics. Time-domain simulations using these synthetic impedance circuits are compared to the ideal frequency-domain results with very good agreement.**

***Index Terms*—Metamaterials, piezoelectricity, piezoelectric devices, vibrations, vibration control.**

I. Introduction

METAMATERIALS and finite metastructures (with specified boundary conditions) [1] made from piezoelectric materials connected to shunt circuits have the potential to be multifunctional and adaptable, since their structural properties are directly affected by the shunt circuits [2]. The use of shunt circuitry has many benefits over purely mechanical structures, such as reduced mass addition and significantly greater design freedom. There is a rich history of research on using piezoelectric materials for vibration attenuation and control [3]–[11], both using active and passive control schemes. More recently, piezoelectric elements with shunt circuits have been applied to metamaterial and metastructure systems, focusing instead on how the effective mechanical properties of the structure are changed by the shunt circuitry. Researchers have considered the use of negative capacitance [13]–[18] and resonant circuits [19]–[22], with an emphasis on reducing vibrations or creating bandgaps. In short, the use of a sufficient number of piezoelectric elements and shunt circuits results in stiffness of the structure being altered by the shunt circuit admittance, limited by the electromechanical coupling of the system [1].

One promising path forward in research on electromechanical metastructures lies in the use of synthetic impedance circuits, a type of voltage-controlled current source that establishes an arbitrary impedance between two terminals. Voltage is measured as an input to a digital signal processing (DSP) system, and a corresponding voltage is applied to obtain the desired current (in that sense, it is in fact synthetic *admittance*). Fleming *et al.* [23] first proposed a simple single-sided synthetic impedance circuit for use in piezoelectric shunt damping, and recently Matten *et al.* [24] and Nečásek *et al.* [25] have successfully developed a synthetic impedance system with piezoelectric elements. This is especially promising for use with electromechanical metastructures, where the impedance applied to each shunt circuit can dramatically change the effective dynamic properties of the structure, and hence its dynamic performance. Ultimately, this technology would enable truly multifunctional and adaptable electromechanical metastructures, whose stiffness could be programed by changing the digital transfer function implemented on a controller.

Previously, we developed the theory for a piezoelectric bimorph beam with segmented electrode pairs as a locally resonant electroelastic metastructure [1]. We showed that if the same normalized admittance is applied to each pair of electrodes and if there are a sufficient number of electrodes, the normalized admittance directly affects the dynamic stiffness of each mode

Manuscript received December 27, 2017; revised May 7, 2018; accepted July 30, 2018. Date of publication August 6, 2018; date of current version October 15, 2018. Recommended by Technical Editor J. Tang. This work was supported by the Air Force Office of Scientific Research "Integrated multi-field resonant metamaterials for extreme, low frequency damping" under Grant FA9550-15-1-0397. *(Corresponding author: Alper Erturk.)*

C. Sugino and A. Erturk are with the G. W. Woodruff School of Mechanical Engineering, Georgia Institute of Technology, Atlanta, GA 30332 USA (e-mail: csugino@gatech.edu; alper.erturk@me.gatech.edu).

M. Ruzzene is with the D. Guggenheim School of Aerospace Engineering, Atlanta, GA 30332 USA, and also with the G. W. Woodruff School of Mechanical Engineering, Georgia Institute of Technology, Atlanta, GA 30332 USA (e-mail: ruzzene@gatech.edu).

Color versions of one or more of the figures in this paper are available online at http://ieeexplore.ieee.org.

Digital Object Identifier 10.1109/TMECH.2018.2863257

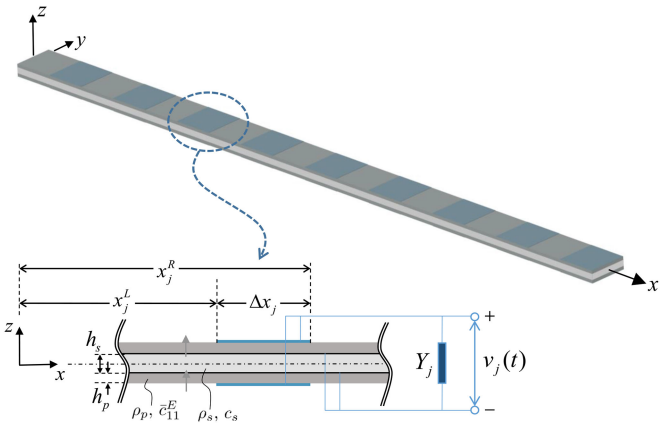

Fig. 1. Schematic of a piezoelectric metastructure (i.e., a finite metamaterial with certain boundary conditions) and a close-up showing the jth electrode pair shunted to an electrical load of admittance Y_j. Since periodicity is not required, the electrode pairs do not have to be identical. Symmetrically located piezoelectric layers are connected in parallel for transverse vibrations (poling directions are shown by gray arrows).

shape of the structure. In the present paper, we develop a general method for designing that normalized admittance to obtain a desired structural response using the root locus method. Poles and zeros can be placed to obtain a particular structural response according to geometric root locus rules, and the corresponding shunt circuit admittance is easily obtained. Case studies for design are shown for creating one or two locally resonant bandgaps of arbitrary width. In order to justify the use of these arbitrary admittances that often require a power input to the system, simulations are performed for a metamaterial beam with synthetic impedance shunts [23], accounting for the finite sampling rate and circuit dynamics.

II. Piezoelectric Metamaterial Beam

Consider a bimorph piezoelectric metamaterial beam with a rectangular cross section made from two continuous and symmetrically located piezoelectric layers sandwiching a central structural (i.e., shim or substrate) layer (see Fig. 1). The piezoelectric layers are poled in the same direction along the transverse axis (for parallel connection). The electrode pairs are segmented (not necessarily in a periodic fashion) into opposing pairs and connected to a total of S shunt circuits. The electrode layers and the bonding layers are assumed to have negligible thickness and effect on both structural and electrical behaviors. The thin composite beam has certain specified boundary conditions and is modeled based on the Euler–Bernoulli beam theory by assuming geometrically small oscillations and linear-elastic material behavior (i.e., piezoelectric material and geometric nonlinearities [26]–[28] are assumed to be negligible). The beam is assumed to be undamped at this point, with the understanding that modal damping can be added easily.

Under these conditions, it can be shown that the governing electromechanical equations of the system for transverse vibrations are

$$\mathrm{EI}\frac{\partial^4 w}{\partial x^4} + m\frac{\partial^2 w}{\partial t^2} - \vartheta \sum_{j=1}^{S} v_j(t)\frac{\partial^2}{\partial x^2}\left[H(x-x_j^L) - H(x-x_j^R)\right] = f(x,t) \tag{1}$$

$$C_{p,j}\frac{\mathrm{d}v_j}{\mathrm{d}t} + \mathscr{Y}_j\left[v_j(t)\right] + \vartheta\int_{x_j^L}^{x_j^R}\frac{\partial^3 w}{\partial x^2 \partial t}dx = 0, \quad j = 1,2,\ldots,S \tag{2}$$

where $w(x,t)$ is the transverse displacement of the beam at position x and time t, $v_j(t)$ is the voltage between the jth electrode pair and the central shim, $H(x)$ is the Heaviside function, and $\mathscr{Y}_j$ is a linear integro-differential operator corresponding to the admittance of the jth shunt circuit. Furthermore, EI is the short-circuit flexural rigidity, m is the mass per length, ϑ is the electromechanical coupling term in physical coordinates, and $C_{p,j}$ is the internal piezoelectric capacitance associated with the jth electrode pair

$$\mathrm{EI} = \frac{2b}{3}\left(c_s\frac{h_s^3}{8} + \bar{c}_{11}^E\left[\left(h_p + \frac{h_s}{2}\right)^3 - \frac{h_s^3}{8}\right]\right) \tag{3}$$

$$m = b(\rho_s h_s + 2\rho_p h_p) \tag{4}$$

$$\vartheta = \bar{e}_{31} b_e (h_s + h_p) \tag{5}$$

$$C_{p,j} = \frac{2\bar{\varepsilon}_{33}^S b_e \left(x_j^R - x_j^L\right)}{h_p} \tag{6}$$

where c_s, ρ_s, and h_s are the central substrate layer's elastic modulus, mass density, and thickness, respectively, and b is the width of the beam. The piezoelectric layers have mass density ρ_p, thickness h_p, width b, elastic modulus at constant electric field $\bar{c}_{11}^E$, effective piezoelectric stress constant $\bar{e}_{31}$, and permittivity component at constant strain $\bar{\varepsilon}_{33}^S$, where the overbars indicate effective material properties for one-dimensional thin layers reduced from three-dimensional constitutive equations as

$$\bar{c}_{11}^E = \frac{1}{s_{11}^E}, \quad \bar{e}_{31} = \frac{d_{31}}{s_{11}^E}, \quad \bar{\varepsilon}_{33}^S = \varepsilon_{33}^T - \frac{d_{31}^2}{s_{11}^E} \tag{7}$$

where s_{11}^E is the elastic compliance at constant electric field, d_{31} is the piezoelectric strain constant, and ε_{33}^T is the permittivity component at constant stress. The piezoelectric layers have segmented surface electrodes numbered $j = 1,2,\ldots,S$, with each electrode starting at $x = x_j^L$ and ending at x_j^R, with total length $\Delta x_j = x_j^R - x_j^L$ (see Fig. 1), and width b_e, symmetric about the xz-plane.

Using an assumed modes-type expansion with N modes, the transverse displacement of the beam is

$$w(x,t) = \sum_{r=1}^{N}\phi_r(x)\eta_r(t) \tag{8}$$

where $\eta_r(t)$ are the modal coordinates to be determined. The mode shapes $\phi_r(x)$ of the beam obtained for a given set of mechanical boundary conditions at short circuit (with a single

electrode pair covering the entire beam) are normalized such that

$$\int_0^L m\phi_r(x)\phi_s(x) = \delta_{rs}, \quad r,s = 1,2,\ldots,N \tag{9}$$

$$\int_0^L \mathrm{EI}\frac{\mathrm{d}^2\phi_r}{\mathrm{d}x^2}\frac{\mathrm{d}^2\phi_s}{\mathrm{d}x^2}dx = \omega_r^2\delta_{rs}, \quad r,s = 1,2,\ldots,N \tag{10}$$

where L is the length of the beam, ω_r is the rth natural frequency, and δ_{rs} is the Kronecker delta. Substituting (8) into (1), multiplying by some mode shape $\phi_k(x)$, and integrating across the beam (see [29] for a full derivation with a single electrode, which can be easily extended to multiple electrodes), governing equations can be obtained in modal coordinates as

$$\ddot{\eta}_r(t) + \omega_r^2\eta_r(t) - \vartheta\sum_{j=1}^{S} v_j(t)\Delta\phi'_{r,j} = q_r(t) \tag{11}$$

$$C_{p,j}\dot{v}_j(t) + \mathscr{Y}_j\left[v_j(t)\right] + \vartheta\sum_{r=1}^{N}\Delta\phi'_{r,j}\dot{\eta}_r(t) = 0 \tag{12}$$

where the free indices r and j are assumed to go from $1,2,\ldots,N$ and $1,2,\ldots,S$, respectively,

$$\Delta\phi'_{r,j} = \left(\frac{\mathrm{d}\phi_r}{\mathrm{d}x}\right)_{x_j^L}^{x_j^R} = \frac{\mathrm{d}\phi_r}{\mathrm{d}x}(x_j^R) - \frac{\mathrm{d}\phi_r}{\mathrm{d}x}\left(x_j^L\right) \tag{13}$$

is the difference in slope of the rth mode between the ends of the jth electrode pair, and

$$q_r(t) = \int_0^L f(x,t)\phi_r(x)dx \tag{14}$$

is the modal forcing. Taking the Laplace transforms of (11) and (12) and substituting (12) into (11), and assuming there are a sufficient number of electrodes on the structure so that the following Riemann sum approximates the orthogonality integral in (10)

$$\sum_{j=1}^{S}\mathrm{EI}\frac{\Delta\phi'_{r,j}}{\Delta x_j}\frac{\Delta\phi'_{k,j}}{\Delta x_j}\Delta x_j \approx \int_0^L \mathrm{EI}\frac{\mathrm{d}^2\phi_r}{\mathrm{d}x^2}\frac{\mathrm{d}^2\phi_k}{\mathrm{d}x^2}dx = \omega_r^2\delta_{rk} \tag{15}$$

it can be shown [1] that the response of the rth mode shape in (8) is given by

$$H_r(s) = \frac{Q_r(s)}{s^2 + \omega_r^2\left(1 + \dfrac{\alpha s}{s + h(s)}\right)} \tag{16}$$

where $H_r(s)$ is the Laplace transform of $\eta_r(t)$ and $Q_r(s)$ is the Laplace transform of $q_r(t)$

$$\alpha = \frac{\vartheta^2 h_p}{2EI\bar{\varepsilon}_{33}^S b_e} = \frac{\bar{e}_{31}^2 b_e h_p(h_s + h_p)^2}{2EI\bar{\varepsilon}_{33}^S} \tag{17}$$

is a dimensionless parameter related to the electromechanical coupling, and

$$h(s) = \frac{Y_j(s)}{C_{p,j}} \tag{18}$$

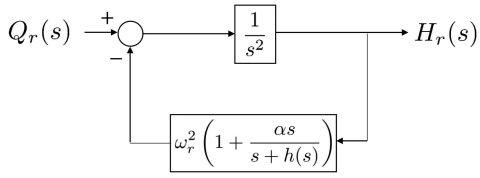

Fig. 2. Equivalent block diagram for the transfer function given in (19).

is the normalized circuit admittance, where Y_j is the admittance of the jth shunt circuit, or equivalently the Laplace transform of $\mathscr{Y}_j$. In order to make this simplification, the normalized circuit admittance $h(s)$ is assumed to be identical for every electrode pair. Clearly, the shunt circuits have added frequency dependence to the modal stiffness of each mode. The extent of the frequency dependence is determined by α, the dimensionless system-level electromechanical coupling term, and the specific form of dependence is determined by $h(s)$, the normalized shunt circuit admittance applied to every shunt circuit.

Note that the approximation in (15) governs how the metastructure with a finite number of segmented electrode pairs begins to behave as an infinite metamaterial (i.e., a unit cell with periodic boundary conditions) as the number of electrode pairs becomes very large. In practice, for relatively low target frequencies (i.e., low modal neighborhoods), it is straightforward to determine how many electrode pairs are required, which is discussed in detail in [1].

III. General Shunt Circuit Design

One of the benefits of using shunt circuits as opposed to mechanical resonators is the great flexibility in obtaining the desired admittance $h(s)$. This is especially true for systems using synthetic impedance, in which $h(s)$ is determined by a digital transfer function implemented on a controller. For this purpose, it is desirable to have a methodology for obtaining the required admittance $h(s)$ for certain design characteristics, such as creating damping in a specified frequency range or creating multiple bandgaps. To this end, the root locus method for system design can provide a quick insight into the structure's response. In the following, it is assumed that there are a sufficient number of electrode pairs to achieve convergence to the approximation in (15) in the desired frequency range.

Consider the transfer function between the rth modal excitation and the rth modal response

$$\frac{H_r(s)}{Q_r(s)} = \frac{1}{s^2 + \omega_r^2\left(1 + \dfrac{\alpha s}{s + h(s)}\right)}. \tag{19}$$

This can be represented by the equivalent block diagram shown in Fig. 2. The characteristic equation of the system is

$$1 + \omega_r^2 G(s)H(s) = 0 \tag{20}$$

where

$$G(s)H(s) = \frac{1}{s^2}\left(\frac{(1+\alpha)s + h(s)}{s + h(s)}\right). \tag{21}$$

To determine the effect of $h(s)$ on each mode of the system, we apply classical root locus techniques with the squared short-circuit natural frequency $\omega_r^2 > 0$ as the varied parameter [30]. The poles and zeros of the transfer function $G(s)H(s)$ determine how the poles and zeros of the full transfer function $H_r(s)/Q_r(s)$ evolve as ω_r^2 is increased. Since there are an infinite number of modes with increasing natural frequencies ω_r, the transfer function $G(s)H(s)$ should be designed in a way that is stable for all values of $\omega_r^2 > 0$, i.e., all of the branches of the root locus must lie exclusively in the left half of the s-plane. Conditional stability is generally not desirable, unless extreme care is taken such that no particular actual mode (i.e., a specific value of ω_r for the structure under consideration) goes unstable. Note that the actual structural response for harmonic excitation [to obtain some desired frequency response function (FRF)] is obtained by summing the modal contributions along the imaginary axis, i.e.,

$$\bar{w}(x,\omega) = \sum_{r=1}^{N} H_r(j\omega)\phi_r(x) \tag{22}$$

where $\bar{w}$ is the vibration amplitude at some point x along the beam at an excitation frequency ω. The poles and zeros of $H_r(s)$ determine the behavior of $H_r(j\omega)$, e.g., poles close to the imaginary axis correspond to resonant frequencies, and zeros close to the imaginary axis correspond to antiresonances.

Because $h(s)$ appears in both the numerator and denominator of $G(s)H(s)$ in (21), there are always two more poles than zeros, implying that the root locus always has two asymptotes at $\pm 90^\circ$ from the positive real axis. This follows the physical intuition that the resonant frequencies of the full system, and thus the imaginary part of at least two poles of the system, must become arbitrarily large as ω_r^2 is increased. That is, as we consider higher and higher modes, there is at least one associated resonance for each mode that becomes arbitrarily large. Additionally, it is always the case that the damping ratio of these two asymptotic poles will become arbitrarily small for higher modes, as they can only have a finite (negative) real part. Without the loss of generality, we can write $G(s)H(s)$ in the more convenient form

$$G(s)H(s) = \frac{K\prod_{i=1}^{n}(s-z_i)}{s^2\prod_{i=1}^{n}(s-p_i)} = \frac{K}{s^2}\frac{N(s)}{D(s)} \tag{23}$$

where

$$N(s) = \prod_{i=1}^{n}(s-z_i), \quad D(s) = \prod_{i=1}^{n}(s-p_i) \tag{24}$$

are polynomials defining the poles and zeros of $G(s)H(s)$ contributed by $h(s)$, K is a constant that does not affect the position of the poles and zeros, n is the total number of zeros of $G(s)H(s)$, and z_i and p_i are the n zeros and poles contributed by $h(s)$, respectively. As mentioned previously, note that the total number of poles of $G(s)H(s)$ is always $n+2$, due to the double pole at the origin. The normalized admittance $h(s)$ required to obtain the form of (23) is given by

$$h(s) = s\left(\frac{(1+\alpha)D(s) - KN(s)}{KN(s) - D(s)}\right). \tag{25}$$

Generally, if $h(s)$ is to be implemented using a digital control system, it is desirable to choose K such that $h(s)$ is a proper transfer function or that $h(s)$ has at least as many poles as zeros. Fortunately, since $N(s)$ and $D(s)$ are always polynomials of the same order, the highest order term of s may always be canceled in the numerator of (25) by selecting $K = 1+\alpha$. Under this simplification, (25) becomes

$$h(s) = \frac{s\left(\prod_{i=1}^{n}(s-p_i) - \prod_{i=1}^{n}(s-z_i)\right)}{\prod_{i=1}^{n}(s-z_i) - \frac{1}{1+\alpha}\prod_{i=1}^{n}(s-p_i)} \tag{26}$$

which will *always* be a proper transfer function, since the maximum order of the numerator is n, and the denominator will always be order n for $\alpha > 0$. Equation (26) can be used to obtain the normalized admittance required to place the desired poles and zeros p_i and z_i of $G(s)H(s)$ for a particular design. Note that, although it is impossible to know the true value of α for a particular system, it can be measured experimentally by comparing open and short-circuit natural frequencies via

$$\alpha = \left(\frac{\omega_{OC,i}}{\omega_{SC,i}}\right)^2 - 1 \tag{27}$$

which should be identical for modes of the structure up to and including the frequency range of interest, assuming a sufficient number of electrode pairs. Equation (27) can be obtained directly from (16) by taking the limits as $h(s) \to \infty$, corresponding to short circuit, and $h(s) \to 0$, corresponding to open circuit, and comparing the roots of the denominator. This is a source of some practical concern, as the estimate of α is required in the transfer function $h(s)$. To investigate the effect of this uncertainty, say an estimate α_{exp} is made that is not quite equal to the true value α for a particular system. Then, using α_{exp} in (26) and substituting into (21) (with the true value α) gives

$$G(s)H(s) = \frac{(1+\alpha)N(s) + \epsilon D(s)}{s^2 D(s)} \tag{28}$$

where $\epsilon = 1 - \alpha/\alpha_{\text{exp}}$ is some small constant. Comparing (23) and (28), it is clear that we obtain the desired performance only when $\alpha_{\text{exp}} = \alpha$ or $\epsilon = 0$. In the presence of small errors, we can expect that the designed poles and zeros will be moved slightly. For a more thorough analysis, the sensitivity of the poles and zeros of $G(s)H(s)$ to the parameter ϵ can be checked to ensure that the system will not be made unstable in the presence of a small uncertainty. Clearly, some care should be taken so that the system poles and zeros are not overly sensitive to ϵ.

Using the well-known geometric rules of the root locus, some stability constraints can be placed on the placement of the poles p_i and zeros z_i. In order to maintain stability at large values of ω_r^2, we have the necessary condition that the intersection of the two asymptotes with the real axis is less than or equal to zero, or

$$\sigma = \frac{\sum_{i=1}^{n} p_i - \sum_{i=1}^{n} z_i}{2} \leq 0 \quad \Rightarrow \quad \sum_{i=1}^{n} p_i \leq \sum_{i=1}^{n} z_i. \tag{29}$$

Additionally, since all branches of the root locus terminate at asymptotes or zeros of $G(s)H(s)$, there can be no zeros in the

right half-plane, or

$$\mathrm{Re}\{z_i\} \leq 0, \quad i = 1, 2, \ldots, n. \tag{30}$$

Since all branches of the root locus begin at the poles of $G(s)H(s)$, it is also generally necessary for all poles to lie in the left half-plane, except in very special cases of conditional stability. Since conditional stability is not desirable, as a general rule, we should require

$$\mathrm{Re}\{p_i\} \leq 0, \quad i = 1, 2, \ldots, n. \tag{31}$$

Finally, in order to maintain real coefficients in both $N(s)$ and $D(s)$, all complex poles and zeros must appear in conjugate pairs. For a more complete check for stability, the full root locus plot can be used, or other criteria such as the Routh–Hurwitz or Nyquist stability criteria. When $h(s)$ requires energy input (e.g., for negative capacitance shunting), stability should be a primary design consideration.

Once the poles and zeros have been selected, it can be checked immediately if $h(s)$ is realizable with a passive network. Consider the normalized impedance associated with the shunt circuit admittance $h(s)$

$$Z(s) = \frac{1}{h(s)}. \tag{32}$$

The necessary and sufficient conditions for physical realization with a passive network are given by Brune [31] as (1) $Z(s)$ is a rational function which is real for real values of s and (2) the real part of $Z(s)$ is positive when the real part of s is positive. The first condition is met automatically by our design method for $h(s)$ by placing poles and zeros in complex conjugate pairs, but the second condition will not generally be true. It is possible that some designs will always require power input, regardless of the specific placement of poles and zeros. The use of a synthetic impedance system will *always* require power input, even if the implemented impedance is passively realizable, because the current output is achieved by applying a voltage over a reference resistor.

The following sections will discuss some of the interesting design possibilities for the normalized shunt admittance $h(s)$ such as negative capacitance, resistive loading, and the purely passive locally resonant bandgap, as well as more complex designs that are easily obtained by placing poles and zeros such as multiple bandgaps. For all structural simulations shown, the beam being considered is a cantilever with length $L = 100$ mm and width $b = 10$ mm, with center shim material aluminum ($c_s = 69$ GPa, $\rho_s = 2700$ kg/m^3, $h_s = 0.1$ mm), and piezoelectric material PIN-PMN-PT, with $\bar{c}_{11}^E = 13.25$ GPa, $\bar{e}_{31} = -17.71$ C/m^2, $\bar{\varepsilon}_{33}^S = 4.05 \times 10^{-8}$ F/m, $\rho_p = 8198$ kg/m^3, $b_e = b = 10$ mm, and $h_p = 0.3$ mm, such that the dimensionless coupling is $\alpha = 0.485$.

A. Negative Capacitance

The use of negative capacitance in parallel with other circuit components has the effect of increasing the effective value of the dimensionless coupling term α, a result that has been discussed previously in the literature [32], [33]. The negative capacitance circuit simulates the effect of having more energy output from the piezoelectric layers, increasing the effective conversion efficiency; of course, this additional energy must be supplied to the system by an outside source. The general form for the normalized admittance of some other normalized admittance $g(s)$ placed in parallel with a negative capacitance circuit is

$$h(s) = g(s) - cs \tag{33}$$

where $0 < c < 1$ indicates the fraction of piezoelectric capacitance being provided by the negative capacitance circuit. Substituting (33) into (21) yields

$$G(s)H(s) = \frac{1}{s^2}\left(\frac{(1+\alpha_{\mathrm{nc}})s + g_{\mathrm{nc}}(s)}{s + g_{\mathrm{nc}}(s)}\right) \tag{34}$$

where

$$\alpha_{\mathrm{nc}} = \frac{\alpha}{1-c}, \quad g_{\mathrm{nc}}(s) = \frac{g(s)}{1-c} \tag{35}$$

are the equivalent electromechanical coupling and normalized circuit admittance of the circuit. That is, the circuit with a parallel negative capacitance is equivalent to a circuit with normalized admittance $g_{\mathrm{nc}}(s)$ with increased electromechanical coupling α_{nc}. This indicates that assuming the negative capacitance shunt is used simply in parallel with the other circuit components, the presence of the negative capacitance will not change the qualitative behavior of the system. This will be illustrated more clearly in the context of the locally resonant bandgap. This analysis also suggests that it is detrimental to have any parallel *positive* capacitance between the two electrodes not due to the piezoelectric, as this would reduce the effective coupling parameter (i.e., set c to some negative number). Note that it is often simpler to place the desired poles and zeros using (26), which will automatically handle any required negative capacitance. On the other hand, it may be beneficial to place a dedicated negative capacitance circuit in parallel with the synthetic impedance circuit to increase the effective value of α for the synthetic impedance circuit.

B. Purely Resistive Load

Using the root locus approach for circuit design, a purely resistive load $h(s) = 1/\tau$, where $\tau = RC_{p,j}$ is the *RC* time constant of each shunt circuit, yields

$$G(s)H(s) = \frac{1}{s^2}\left(\frac{(1+\alpha)\tau s + 1}{\tau s + 1}\right) \tag{36}$$

such that the shunt circuitry acts as a lead compensator, adding a negative real pole and zero to the system, i.e.,

$$\text{Pole:} \quad s = -\frac{1}{\tau}, \quad \text{Zero:} \quad s = -\frac{1}{\tau(1+\alpha)} \tag{37}$$

such that the pole is always less than the zero. As with a typical lead compensator, this has the effect of pulling the root locus to the left, adding damping and stability to the system (see Fig. 3) along with the corresponding structural FRF.

The total shift in the asymptote intersection σ contributed by the lead compensator is

$$\Delta\sigma = \frac{1}{2}\left(-\frac{1}{\tau} + \frac{1}{\tau(1+\alpha)}\right) = -\frac{\alpha}{2\tau(1+\alpha)}. \tag{38}$$

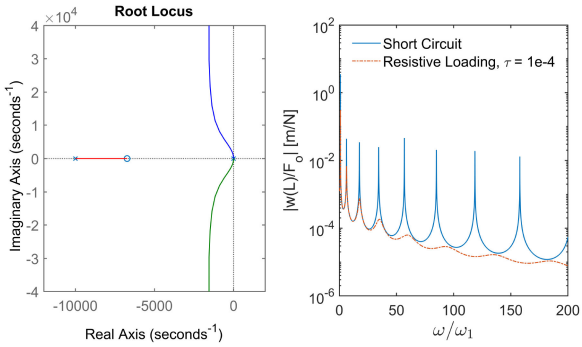

Fig. 3. Typical root locus plot of the poles of $H_r(s)/Q_r(s)$ with varying parameter $\omega_r^2 > 0$ (left), and corresponding response FRF (right) for a cantilever beam with a harmonic point force excitation of magnitude F_o and frequency ω at $x = 0.1L$. Both plots use $\tau = 1 \times 10^{-4}$ s, and the resulting damping is clearly visible at high frequencies in the FRF.

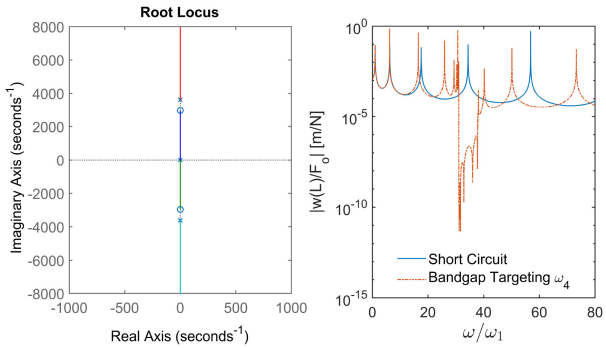

Fig. 4. Typical root locus plot for a locally resonant bandgap (left), and corresponding response FRF (right) for a cantilever beam with a point force excitation of magnitude F_o at $x = 0.1L$. Both plots use a target frequency $\omega_t = 1.1\omega_4$, such that the resulting bandgap targets the fourth short-circuit natural frequency. Note also the many resonances that appear before the bandgap, which can be mitigated by adding damping to $h(s)$.

Larger values of α or smaller values of τ increase the separation between the pole and zero added by the lead compensator such that the root locus moves farther into the left half-plane. Note that for very high frequency modes, the effect of the pole and zero on the real axis is effectively canceled, leaving only the added damping from the asymptote shift. This added damping also becomes small for higher modes, since the real component is fixed.

C. Locally Resonant Bandgap

The locally resonant bandgap is obtained by using a purely inductive load, yielding $h(s) = \omega_t^2/s$, where ω_t is the resonant frequency of the *LC* circuit. The corresponding form of $G(s)H(s)$ is

$$G(s)H(s) = \frac{1}{s^2}\left(\frac{s^2(1+\alpha)+\omega_t^2}{s^2+\omega_t^2}\right) \tag{39}$$

such that zeros are added at $s = \pm j\omega_t/\sqrt{1+\alpha}$ and poles are added at $s = \pm j\omega_t$. Thus, there can be no branches of the root locus with imaginary part between $\omega_t/\sqrt{1+\alpha}$ and ω_t, i.e., the frequency range

$$\frac{\omega_t}{\sqrt{1+\alpha}} < \omega < \omega_t \tag{40}$$

defines the locally resonant bandgap. The dimensionless electromechanical coupling term α determines the width of the bandgap, with larger values of α yielding wider bandgaps. A typical root locus and the corresponding structural response are shown in Fig. 4. The multiple additional valleys inside the locally resonant bandgap can be attributed to the particular modes of the structure being considered (here a cantilever) and largely disappear with the addition of damping to the shunt circuits.

Note that if $h(s)$ is to be implemented using DSP, it is likely necessary to add some damping to both the pole and zero of $h(s)$ to maintain stability. This can be achieved by placing a resistor in parallel with the inductance, or equivalently using

$$h(s) = \frac{\omega_t^2}{s} + 2\zeta\omega_t \tag{41}$$

for some desired damping ratio ζ. This also has the benefit of attenuating the many resonant frequencies that occur before the locally resonant bandgap, which are visible in Fig. 4, without significantly reducing the attenuation in the bandgap itself. The corresponding poles and zeros of $G(s)H(s)$ are

$$\text{Poles:} \quad s = \omega_t\left(-\zeta \pm \sqrt{\zeta^2-1}\right) \tag{42}$$

$$\text{Zeros:} \quad s = \frac{\omega_t}{1+\alpha}\left(-\zeta \pm \sqrt{\zeta^2-(1+\alpha)}\right). \tag{43}$$

An alternative approach to improve stability and attenuate the edge resonances would be to add a lead compensator to the system in analogy with the purely resistive load as discussed in Section III-B.

As mentioned previously, the use of negative capacitance can increase the effective value of α. In the context of the locally resonant bandgap, this would increase the width of the bandgap by reducing the lower edge frequency. More specifically, assuming the same target frequency ω_t, the effective bandgap with negative capacitance is

$$\frac{\omega_t}{\sqrt{1+\alpha/(1-c)}} < \omega < \omega_t. \tag{44}$$

This expression suggests that the lower edge frequency of the bandgap can be made arbitrarily close to zero by using $c \to 1$. This is an idealization, as the system would likely be unstable and require very large power input. For the case of a single bandgap, the effect of negative capacitance is easily understood via its effect on the coupling term α. For more complex systems, it is typically simpler to place the poles and zeros to obtain the desired performance (e.g., multiple bandgaps), then use (26) to find the required shunt admittance.

D. Multiple Bandgaps

Bandgaps are characterized by the absence of resonant frequencies across a wide frequency range. In terms of the root locus, we require a certain alternating arrangement of poles and zeros on the imaginary axis. In general, to create n_b bandgaps between lower and upper edge frequencies $\omega_{i,l}$ and $\omega_{i,u}$, we

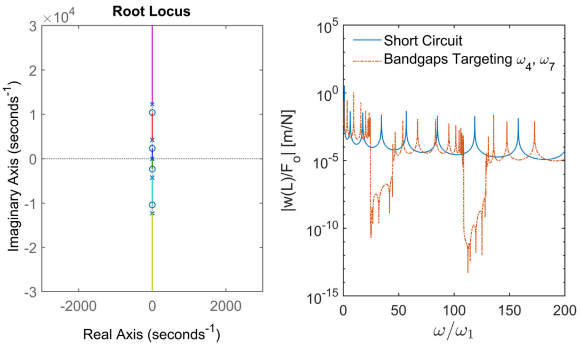

Fig. 5. Typical root locus plot for two bandgaps (left), and corresponding response FRF (right) for a cantilever beam with a point force excitation of magnitude F_o at $x = 0.1L$. Bandgaps were placed to attenuate the response at the fourth and seventh natural frequencies of the structure at short circuit.

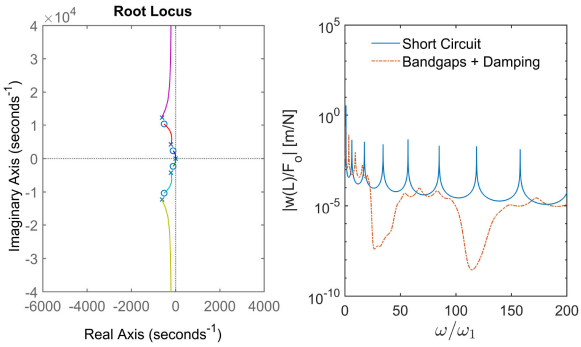

Fig. 6. Typical root locus plot for two bandgaps with damping (left), and corresponding response FRF (right) for a cantilever beam with a point force excitation of magnitude F_o at $x = 0.1L$. Bandgaps were placed to attenuate the response at the fourth and seventh natural frequencies of the structure at short circuit, and 5% damping was added to each pole and zero.

require

$$N(s) = \prod_{i=1}^{n_b}(s^2 + \omega_{i,l}^2), \quad D(s) = \prod_{i=1}^{n_b}(s^2 + \omega_{i,u}^2) \tag{45}$$

with the constraint

$$0 < \omega_{1,l} < \omega_{1,u} < \omega_{2,l} < \omega_{2,u} < \cdots < \omega_{n_b,l} < \omega_{n_b,u} \tag{46}$$

such that there is an alternating pattern of poles and zeros along the imaginary axis, with the zeros corresponding to the lower edge frequencies and poles corresponding to upper edge frequencies. An example root locus with two bandgaps is shown in Fig. 5 along with the corresponding structural response FRF, with bandgaps placed to attenuate the response at the fourth and seventh natural frequencies of the structure at short circuit.

It can be expected that nearly all systems with multiple bandgaps will require power input to the system. As with the single locally resonant bandgap, it is likely necessary to add some damping to maintain stability for digital implementations of the transfer function. This can be achieved as before by adding some damping to each pair of poles and zeros, i.e.,

$$N(s) = \prod_{i=1}^{n_b}\left(s^2 + 2\zeta_i\omega_{i,l} + \omega_{i,l}^2\right),$$

$$D(s) = \prod_{i=1}^{n_b}\left(s^2 + 2\zeta_i\omega_{i,u} + \omega_{i,u}^2\right) \tag{47}$$

where ζ_i is the damping ratio of the ith bandgap. It is not necessary to give the same damping factor to both the pole and zero of a particular bandgap, but doing so guarantees that the condition for stability in (29) is met. Note that, although adding damping has the benefit of attenuating the resonances that appear before the bandgap, very large damping ratios will reduce the attenuation in the bandgap as the system's zeros are moved far from the imaginary axis. An example root locus for two bandgaps with 5% damping on every pole and zero, and the corresponding structural response is shown in Fig. 6. Although damping significantly attenuates the resonances that appear before each bandgap, the attenuation in each bandgap has been reduced.

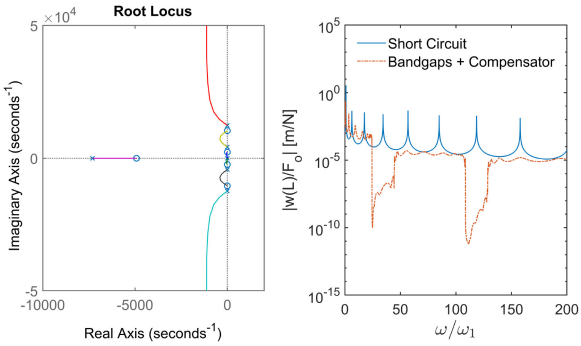

Fig. 7. Typical root locus plot for two bandgaps with damping (left), and corresponding response FRF (right) for a cantilever beam with a point force excitation of magnitude F_o at $x = 0.1L$. Bandgaps were placed to attenuate the response at the fourth and seventh natural frequencies of the structure at short circuit, and a compensator was added to target the center of the frequency range between the two bandgaps.

As with the single bandgap, a compensator can also be used to attenuate the resonances that appear before each bandgap and improve stability, at the cost of increased system complexity (an additional pole and zero are necessary). The corresponding forms of $N(s)$ and $D(s)$ are then

$$N(s) = (s - z)\prod_{i=1}^{n_b}\left(s^2 + \omega_{i,l}^2\right),$$

$$D(s) = (s - p)\prod_{i=1}^{n_b}\left(s^2 + \omega_{i,u}^2\right). \tag{48}$$

From the previous stability analysis, we must have $p < z$ for stability. Of course, damping can be used in addition to lead compensation for increased stability. The placement of pole and zero on the real axis determines the frequency range with the most damping as well as the extent of attenuation. Because the lead compensator does not move the zeros from the imaginary axis, lead compensation does not significantly reduce the sharp attenuation in the bandgap. An example root locus for two bandgaps with a compensator and the corresponding structural response is shown in Fig. 7. It is clear that the resonances

before each bandgap have been significantly reduced, and that the attenuation in each bandgap is effectively unchanged.

E. Modal Damping

Clearly, the root locus interpretation is only possible in the absence of modal damping, since the modal damping term contains ω_r. However, for relatively small modal damping, we can expect that the effect of the shunt circuitry on the structure is much more significant than the effect of damping and continues the design process assuming no modal damping. The effect of damping on any particular mode can be investigated by fixing ω_r^2 and observing the root locus for varying modal damping ratio. The modal transfer function can be easily modified to include modal damping as

$$\frac{H_r(s)}{Q_r(s)} = \frac{1}{s^2 + 2\zeta_r\omega_r s + \omega_r^2\left(1 + \dfrac{\alpha s}{s + h(s)}\right)} \tag{49}$$

where ζ_r is the rth modal damping ratio. For some fixed value of ω_r (for some mode shape of the plain structure), the characteristic equation can be written as

$$1 + \zeta_r\left(\frac{2\omega_r s(s + h(s))}{s^2(s + h(s)) + \omega_r^2\left((1+\alpha)s + h(s)\right)}\right) = 0 \tag{50}$$

and so the root locus can be considered with $\zeta_r > 0$ as the varied parameter. Of course, it can be expected that modal damping will increase the stability of the system, but it may negatively affect the desired structural response (e.g., the attenuation inside the locally resonant bandgap).

IV. Synthetic Impedance Shunts and Case Studies

The previous discussion assumed unlimited flexibility in the design of the shunt circuit, such that $h(s)$ is any transfer function necessary to obtain the desired performance. Fleming *et al.* [23] suggested a two-terminal device that they termed "synthetic impedance" or "synthetic admittance" to implement an arbitrary transfer function between an input voltage and output current. The primary idea is to use a combination of simple circuit elements and DSP to measure the voltage across the piezoelectric element, then output the corresponding voltage across a reference resistor to obtain the desired current. Operational amplifiers are used to buffer and scale the measured voltage and supply the necessary current and power at the output.

A. Metamaterial Piezoelectric Bimorph Beam With Synthetic Impedance Shunts

The synthetic impedance circuit originally suggested by Fleming *et al.* [23] is applied here to a piezoelectric bimorph connected in parallel, which produces a voltage referenced to the floating voltage level of the central shim. The positive terminal of the circuit is connected to the two electrodes, and the negative terminal is connected to the central shim, such that the central shim is virtually grounded for every electrode pair. The full synthetic impedance circuit is shown in Fig. 8.

Time-domain simulations accounting for the full dynamics of each synthetic impedance circuit were run in Simulink. The modal-governing equations (11) and (12) can be written in vector form as

$$\ddot{\boldsymbol{\eta}} + [\Lambda]\boldsymbol{\eta} + [K_{v\to\eta}]\,\boldsymbol{v} = \boldsymbol{K_q}F_o(t) \tag{51}$$

$$\dot{\boldsymbol{v}} + [\mathscr{Y}]\boldsymbol{v} - [K_{\eta\to v}]\,\dot{\boldsymbol{\eta}} = \boldsymbol{0} \tag{52}$$

where

$$\boldsymbol{\eta} = [\,\eta_1 \quad \cdots \quad \eta_N\,]^T, \quad \boldsymbol{v} = [\,v_1 \quad \cdots \quad v_S\,]^T \tag{53}$$

$$[\Lambda] = \mathrm{diag}[\,\omega_1^2 \quad \omega_2^2 \quad \cdots \quad \omega_N^2\,] \tag{54}$$

$$[C_p] = \mathrm{diag}\big[\,C_{p,1} \quad C_{p,2} \quad \cdots \quad C_{p,S}\,\big] \tag{55}$$

$$[\mathscr{Y}] = [C_p]^{-1}\mathrm{diag}\big[\,\mathscr{Y}_1 \quad \mathscr{Y}_2 \quad \cdots \quad \mathscr{Y}_S\,\big] \tag{56}$$

$$[K_{v\to\eta}] = \vartheta\begin{bmatrix} \Delta\phi'_{1,1} & \Delta\phi'_{1,2} & \cdots & \Delta\phi'_{1,S} \\ \Delta\phi'_{2,1} & \ddots & & \vdots \\ \vdots & & \ddots & \vdots \\ \Delta\phi'_{N,1} & \cdots & \cdots & \Delta\phi'_{N,S} \end{bmatrix} \tag{57}$$

$$[K_{\eta\to v}] = -[C_p]^{-1}[K_{v\to\eta}]^T \tag{58}$$

and $\boldsymbol{K_q}$ defines the effect of the excitation $F_o(t)$ on each modal coordinate. For simplicity, a point force excitation $F_o(t)$ was used at a position x_f, such that

$$q_r(t) = F_o(t)\phi_r(x_f) \tag{59}$$

and accordingly

$$\boldsymbol{K_q} = \big[\,\phi_1(x_f) \quad \phi_2(x_f) \quad \cdots \quad \phi_N(x_f)\,\big]^T. \tag{60}$$

The primary block diagram is shown in Fig. 9.

The individual circuit simulations were handled in Simulink using Simscape Electronics. Since the transfer function for each shunt circuit is assumed to be the same, the "For Each" block in Simulink is used to apply the same circuit to each individual pair of electrodes. The subsystems inside each block are shown in Fig. 8, as discussed previously.

To account for analog to digital conversion and digital to analog conversion, a discrete version of the ideal continuous transfer function $Y_j(s)$ was obtained using MATLAB's `c2d` command using the bilinear transform. An input delay of one sample was included to account for calculation time, although the delay of an actual system may vary depending on the complexity of the desired transfer function. The digital sampling rate of the system was selected to maintain stability, but was not optimized to be as low as possible.

For all simulations, $N = 50$ modes and $S = 12$ pairs of electrodes were used to ensure convergence to the approximation in (15). Electrodes were assumed to be segmented in a uniform manner, such that $x_j^L = (j-1)L/S$ and $x_j^R = jL/S$. The structure was assumed to be a cantilever bimorph beam excited by a point force at $x_f = 0.1L$, with PIN-PMN-PT as the piezoelectric material to give relatively large dimensionless coupling $\alpha = 0.485$, with the same parameters as described in Section III. For concreteness, $R_c = 5\,\mathrm{k}\Omega$ was used. Additionally, 1% modal damping was assumed for every mode, i.e., $\zeta_r = 0.01$.

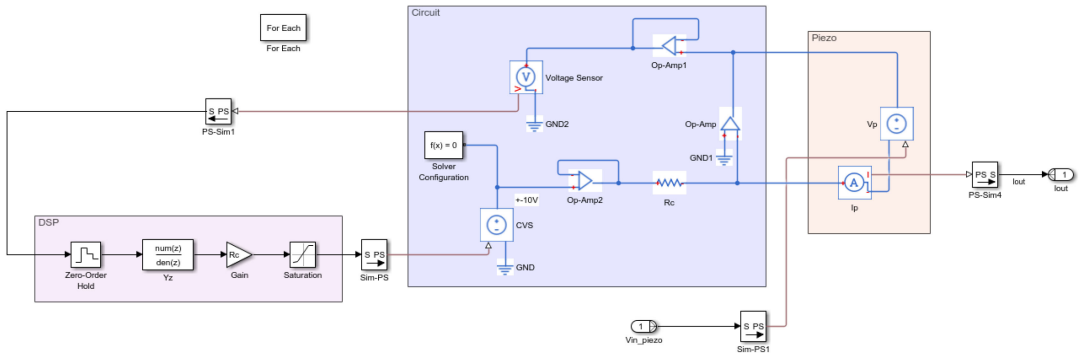

Fig. 8. Block diagram showing the full synthetic impedance circuit. The input to the system is the voltage across the piezoelectric, v_p, and the output is the current through the piezoelectric element, i_{out}, defined according to the passive sign convention. The DSP unit takes the measured voltage from the analog part of the circuit and applies the corresponding input voltage back to the analog circuit.

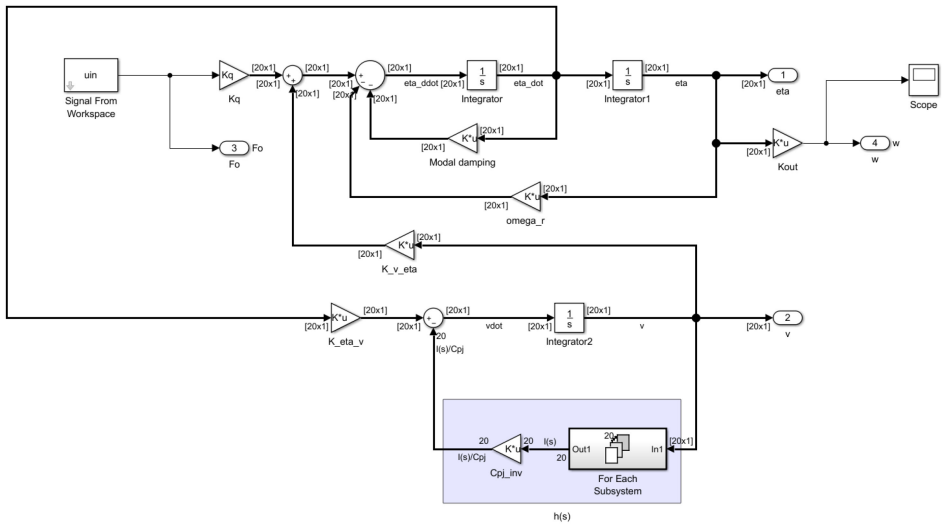

Fig. 9. Simulink block diagram for the governing equations in modal coordinates. The "For Each Subsystem" block contains the voltage dynamics, which are assumed to be the same for each pair of electrodes. The η related signals are $N \times 1$ vectors and the v related signals are $S \times 1$ vectors.

To characterize the performance of the system, FRFs were calculated relating the tip displacement of a cantilever beam to the force input magnitude at $x_f = 0.1L$. A noise burst signal was used as the input, and the corresponding frequency response was obtained using a Hanning window and the Fast Fourier Transform. Because Simscape Electronics automatically includes typical noise sources for each component (e.g., thermal noise from resistors), root mean square averaging over multiple simulations was used to reduce the noise in the FRFs. For each system considered, the ideal model FRFs were obtained from (11) and (12) using matrix inversion, assuming the admittance Y_j is exact.

B. Case Study I: Locally Resonant Bandgap

As discussed in Section III-C, the locally resonant bandgap is obtained by using $h(s) = \omega_t^2/s$. To maintain stability in the presence of some input delay, 5% damping was added, as given in (41). For small damping values, the resulting bandgap should have edge frequencies that agree well with (40). As a case study, the bandgap was designed to be centered on the fifth short-circuit natural frequency of the system, with $\omega_t = 2\omega_5/(1 + 1/\sqrt{1+\alpha})$. The digital sampling rate was set to $f_s = 100$ kHz to maintain stability. In general, a very high digital sampling rate is required to maintain stability, as observed by Nečásek *et al.* [25], although a more thorough analysis is required to pinpoint the precise source of instability. A comparison of the time-domain simulation and the idealized frequency-domain model is shown in Fig. 10, revealing a very good agreement.

C. Case Study II: Locally Resonant Bandgap With Negative Capacitance

As discussed in Section III-A, the use of negative capacitance can effectively increase the coupling factor α. Alternatively, rather than designing negative capacitance separately from the rest of the circuit, the poles and zeros of $h(s)$ can be placed using (26) to create a bandgap that is wider than the purely passive locally resonant bandgap. As a case study, the normalized admittance $h(s)$ was designed to create a bandgap in the frequency range $\omega_5/(2\pi) \pm 200$ Hz. Note that for the purely

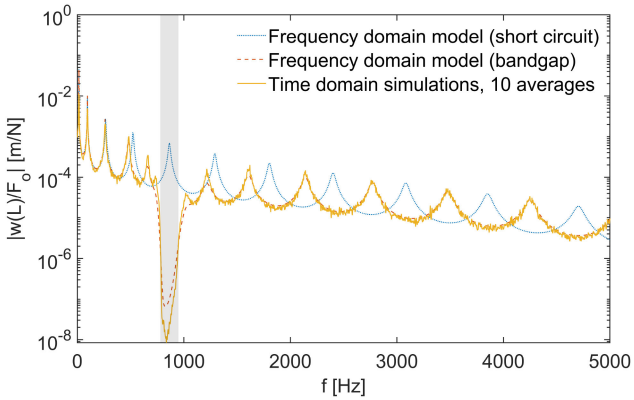

Fig. 10. Comparison of time-domain simulations and frequency-domain simulations for a bandgap targeting the fifth mode of the system at short circuit, with 5% damping on the pole and zero, $S = 12$ electrodes, and $N = 50$ modes. The shaded gray regions indicate the expected infinite-electrode bandgaps. The digital sampling rate was set to 100 kHz, with a one-sample input delay. The short circuit response is included for comparison.

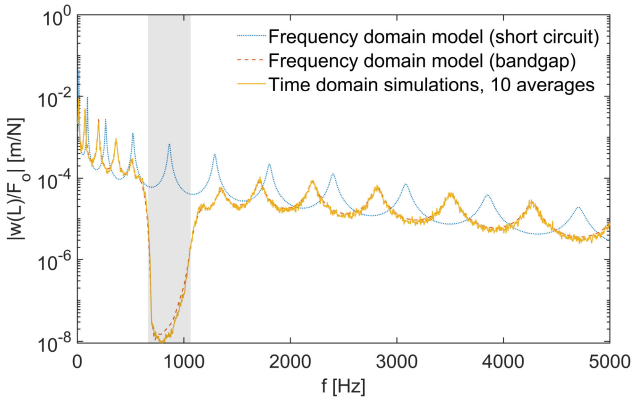

Fig. 11. Comparison of time-domain simulations and frequency-domain simulations for a bandgap targeting ω_5 including negative capacitance, with 5% damping on the pole and zero, $S = 12$ electrodes, and $N = 50$ modes. The shaded gray regions indicate the expected infinite-electrode bandgaps. The digital sampling rate was set to 500 kHz, with a one-sample input delay. The short circuit response is included for comparison.

passive case for this particular system, as shown in Fig. 10, the bandgap centered on ω_5 would only span $\omega_5/(2\pi) \pm 85$ Hz. The digital sampling rate was set to 500 kHz. A comparison of the time-domain simulation and the idealized frequency domain model is shown in Fig. 11; once again, a very good agreement is observed.

D. Case Study III: Multiple Bandgaps

In certain applications, it might be the case that vibration needs to be reduced in frequency ranges that are significantly separated from each other. In these cases, rather than create a single wide bandgap, it may be more efficient to create multiple bandgaps targeting the specific frequency ranges of interest. As a case study, the normalized admittance $h(s)$ was designed to create bandgaps around the fourth and seventh short-circuit natural frequencies of the system, with 5% damping added to each pole and zero. The digital sampling rate was set to 1 MHz. Time-domain simulations and frequency-domain results are shown in Fig. 12 together for this case as well.

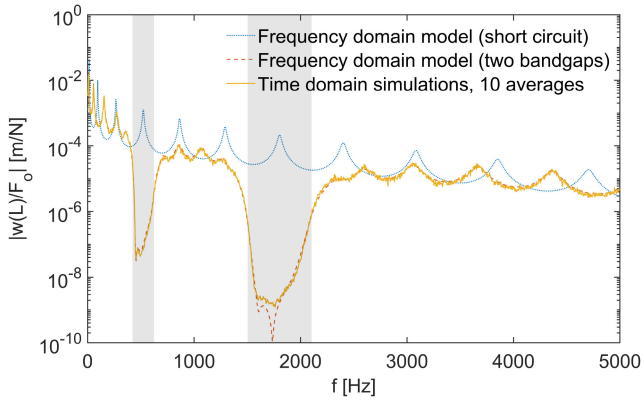

Fig. 12. Comparison of time-domain simulations and frequency-domain simulations for two bandgaps targeting ω_4 and ω_7, with 5% damping on the pole and zero, $S = 12$ electrodes, and $N = 50$ modes. The shaded gray regions indicate the expected infinite-electrode bandgaps. The digital sampling rate was set to 1 MHz, with a one-sample input delay. The short circuit response is included for comparison.

V. Conclusion

Locally resonant piezoelectric metamaterials, and more recently finite metastructures with specified boundary conditions employing inductive shunts, have been well studied over the past decade. Besides the issues related to enabling inductors for low-frequency applications, the resulting bandgap size in locally resonant metamaterials is limited by the system-level electromechanical coupling. To overcome such limitations of simple resonant shunts, the domains of piezoelectric metamaterials and synthetic impedance circuits were coupled in this paper. A general framework was presented for design and analysis of piezoelectric metamaterials and metastructures that employ segmented electrode pairs shunted to synthetic impedance circuits. The focus was placed on a bimorph metamaterial beam undergoing transverse vibrations and a root locus method was employed to design the shunt circuits. Using this approach, poles and zeros can be placed according to the desired structural behavior (e.g., damping, single, or multiple bandgaps), and the corresponding shunt circuit admittance is obtained. This is especially useful for implementation on a system with synthetic impedance for which the admittance is simply implemented as a digital transfer function on a controller. Examples of applications were shown through numerical case studies for adding damping, obtaining a locally resonant bandgap, or creating multiple bandgaps in a cantilevered bimorph metamaterial beam, as a specific metastructure. A synthetic impedance circuit for use with symmetric voltages was developed and simulated in Simulink, yielding good agreement with the predicted FRFs in all cases.

It should be mentioned that there are practical challenges when implementing these synthetic impedance circuits on a segmented bimorph beam. As discussed in Section IV, a very high sampling rate is required to maintain stability, and with

many shunt circuits in a single system, the total required signal throughput can be very large. Additionally, small variations in piezoelectric capacitance must be accounted for, as well as any signal processing delays, which add a phase delay to the intended impedance. For all these reasons, maintaining a stable system with many synthetic shunt circuits can be a significant challenge, but the techniques presented here can provide an insight into preserving stability with complex shunt circuit impedances.

References

[1] C. Sugino, S. Leadenham, M. Ruzzene, and A. Erturk, "An investigation of electroelastic bandgap formation in locally resonant piezoelectric metastructures," *Smart Mater. Struct.*, vol. 26, no. 5, 2017, Art. no. 055029.

[2] G. A. Lesieutre, "Vibration damping and control using shunted piezoelectric materials," *Shock Vib. Dig.*, vol. 30, no. 3, pp. 187–195, 1998.

[3] T. Bailey and J. Hubbard, Jr, "Distributed piezoelectric-polymer active vibration control of a cantilever beam," *J. Guid.*, vol. 8, no. 5, pp. 605–611, 1985.

[4] N. W. Hagood and A. von Flotow, "Damping of structural vibrations with piezoelectric materials and passive electrical networks," *J. Sound Vib.*, vol. 146, no. 2, pp. 242–268, 1991.

[5] J. J. Dosch, D. J. Inman, and E. Garcia, "A self-sensing piezoelectric actuator for collocated control," *J. Intell. Mater. Syst. Struct.*, vol. 3, pp. 166–185, 1992.

[6] M. Arafa and A. Baz, "Dynamics of active piezoelectric damping composites," *Composites Part B: Eng.*, vol. 31, no. 4, pp. 255–264, 2000.

[7] A. J. Fleming, S. Behrens, and S. O. Moheimani, "Optimization and implementation of multimode piezoelectric shunt damping systems," *IEEE/ASME Trans. Mechatronics*, vol. 7, no. 1, pp. 87–94, Mar. 2002.

[8] D. Halim and S. O. Moheimani, "Experimental implementation of spatial H_∞ control on a piezoelectric-laminate beam," *IEEE/ASME Trans. Mechatronics*, vol. 7, no. 3, pp. 346–356, Sep. 2002.

[9] S. O. Moheimani, A. J. Fleming, and S. Behrens, "Dynamics, stability, and control of multivariable piezoelectric shunts," *IEEE/ASME Trans. Mechatronics*, vol. 9, no. 1, pp. 87–99, Mar. 2004.

[10] H. Yu and K. W. Wang, "Vibration suppression of mistuned coupled-blade-disk systems using piezoelectric circuitry network," *J. Vib. Acoust.*, vol. 131, 2009, Art. no. 021008.

[11] W. Zhou and L. Zuo, "A self-powered piezoelectric vibration control system with switch precharged inductor (SPCI) method," *IEEE/ASME Trans. Mechatronics*, vol. 20, no. 2, pp. 773–781, Apr. 2015.

[12] Y. Wu and M. Deng, "Experimental study on robust nonlinear forced vibration control for an L-shaped arm with reduced control inputs," *IEEE/ASME Trans. Mechatronics*, vol. 22, no. 5, pp. 2186–2195, Oct. 2017.

[13] B. S. Beck, K. A. Cunefare, M. Ruzzene, and M. Collet, "Experimental analysis of a cantilever beam with a shunted piezoelectric periodic array," *J. Intell. Mater. Syst. Struct.*, vol. 22, pp. 1177–1187, 2011.

[14] Y. Y. Chen, G. L. Huang, and C. T. Sun, "Band gap control in an active elastic metamaterial with negative capacitance piezoelectric shunting," *J. Vib. Acoust.*, vol. 136, 2014, Art. no. 061008.

[15] S. Behrens, A. J. Fleming, and S. O. Moheimani, "A broadband controller for shunt piezoelectric damping of structural vibration," *Smart Mater. Struct.*, vol. 12, pp. 18–28, 2003.

[16] C. H. Park and A. Baz, "Vibration control of beams with negative capacitive shunting of interdigital electrode piezoceramics," *J. Vib. Control*, vol. 11, no. 3, pp. 331–346, 2005.

[17] B. de Marneffe and A. Preumont, "Vibration damping with negative capacitance shunts: Theory and experiment," *Smart Mater. Struct.*, vol. 17, no. 3, 2008, Art. no. 035015.

[18] R. Zhu, Y. Y. Chen, M. V. Barnhart, G. K. Hu, C. T. Sun, and G. L. Huang, "Experimental study of an adaptive elastic metamaterial controlled by electric circuits," *Appl. Phys. Lett.*, vol. 108, 2016, Art. no. 011905.

[19] F. Casadei, M. Ruzzene, L. Dozio, and K. A. Cunefare, "Broadband vibration control through periodic arrays of resonant shunts: Experimental investigation on plates," *Smart Mater. Struct.*, vol. 19, 2010, Art. no. 015002.

[20] L. Airoldi and M. Ruzzene, "Design of tunable acoustic metamaterials through periodic arrays of resonant shunted piezos," *New J. Phys.*, vol. 13, 2011, Art. no. 113010.

[21] A. E. Bergamini, M. Zundel, E. A. F. Parra, T. Delpero, M. Ruzzene, and P. Ermanni, "Hybrid dispersive media with controllable wave propagation: A new take on smart materials," *J. Appl. Phys.*, vol. 118, no. 15, 2015, Art. no. 154310.

[22] G. Wang and S. Chen, "Large low-frequency vibration attenuation induced by arrays of piezoelectric patches shunted with amplifier-resonator feedback circuits," *Smart Mater. Struct.*, vol. 25, 2015, Art. no. 015004.

[23] A. J. Fleming, S. Behrens, and S. O. Moheimani, "Synthetic impedance for implementation of piezoelectric shunt-damping circuits," *Electron. Lett.*, vol. 36, no. 18, pp. 1525–1526, Aug. 2000.

[24] G. Matten, M. Collet, S. Cogan, and E. Sadoulet-Reboul, "Synthetic impedance for adaptive piezoelectric metacomposite," *Procedia Technol.*, vol. 15, pp. 84–89, 2014.

[25] J. Nečásek, J. Václavik, and P. Marton, "Digital synthetic impedance for application in vibration damping," *Rev. Sci. Instrum.*, vol. 87, 2016, Art. no. 024704.

[26] S. C. Stanton, A. Erturk, B. P. Mann, and D. J. Inman, "Resonant manifestation of intrinsic nonlinearity within electroelastic micropower generators," *Appl. Phys. Lett.*, vol. 97, no. 25, pp. 254101–254103, 2010.

[27] S. Leadenham and A. Erturk, "Unified nonlinear electroelastic dynamics of a bimorph piezoelectric cantilever for energy harvesting, sensing, and actuation," *Nonlinear Dyn.*, vol. 79, no. 3, pp. 1727–1743, 2015.

[28] D. Tan, P. Yavarow, and A. Erturk, "Resonant nonlinearities of piezoelectric macro-fiber composite cantilevers with interdigitated electrodes in energy harvesting," *Nonlinear Dyn.*, vol. 92, no. 4, pp. 1935–1945, 2018.

[29] A. Erturk and D. J. Inman, "An experimentally validated bimorph cantilever model for piezoelectric energy harvesting from base excitations," *Smart Mater. Struct.*, vol. 18, no. 2, 2009, Art. no. 025009.

[30] K. Ogata, *Modern Control Engineering*, 5th ed. Upper Saddle River, NJ, USA: Prentice-Hall (Inc.), 2009.

[31] O. Brune, "Synthesis of a finite two-terminal network whose driving-point impedance is a prescribed function of frequency," *Stud. Appl. Math.*, vol. 10, pp. 1–4, 1931.

[32] J. Tang and K. W. Wang, "Active-passive hybrid piezoelectric networks for vibration control: Comparisons and improvement," *Smart Mater. Struct.*, vol. 10, no. 4, pp. 794–806, 2001.

[33] H. Yu, K. W. Wang, and J. Zhang, "Piezoelectric networking with enhanced electromechanical coupling for vibration delocalization of mistuned periodic structures—theory and experiment," *J. Sound Vib.*, vol. 295, pp. 246–265, 2006.

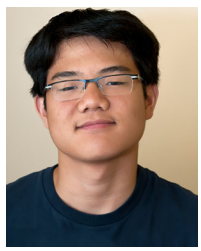

Christopher Sugino received the B.S. degree in engineering from Harvey Mudd College, Claremont, CA, USA, in 2015. He is currently working toward the Ph.D. degree in mechanical engineering at the G. W. Woodruff School of Mechanical Engineering, Georgia Institute of Technology, Atlanta, GA, USA.

He is currently a Graduate Research Assistant with the G. W. Woodruff School of Mechanical Engineering, Georgia Institute of Technology, Atlanta, GA, USA. His research interests include the dynamics of metamaterials/metastructures, structural vibration, and smart structures.

Massimo Ruzzene received his Ph.D. degree in mechanical engineering from Politecnico di Torino, in 1999.

He is the Pratt and Whitney Professor of Aerospace and Mechanical Engineering, Georgia Tech, Atlanata, GA, USA. He has authored or coauthored 2 books, 155 journal papers, and about 180 conference papers, and has participated in projects funded by the AFOSR, ARO, ONR, NASA, US Army, US Navy, DARPA, and NSF, as well as numerous companies. His research interests include solid mechanics, structural dynamics, and wave propagation with application to structural health monitoring, metamaterials, and vibration and noise control.

Prof. Ruzzene is a Fellow of ASME, an Associate Fellow of AIAA, and a member of AHS and ASA.

Alper Erturk received his Ph.D. degree in engineering mechanics from Virginia Tech, in 2009.

He is an Associate Professor and Woodruff Faculty Fellow with the G. W. Woodruff School of Mechanical Engineering, Georgia Institute of Technology, Atlanta, GA, USA, where he leads the Smart Structures and Dynamical Systems Laboratory. He has authored or coauthored 2 books and 200 papers in journals and conference proceedings on topics spanning from vibration energy harvesting and bioinspired actuation to elastic/acoustic metamaterials and phononic crystals.

Prof. Erturk is a Fellow of ASME. He is a recipient of various awards, including an NSF CAREER Award (2013), an ASME Gary Anderson Early Achievement Award (2015), and an ASME C.D. Mote Jr. Early Career Award (2017), among others.